DOI: 10.1002/chem.200701662

Proton-Mediated Redox Control in a Nickel(II)–Bisimidazolate Complex: Spectroscopic Characterisation and Density Functional Analysis

Benedikt Lassalle-Kaiser,[a] Régis Guillot,[a] Joëlle Sainton,[a] Marie-France Charlot,*[a] and Ally Aukauloo*[a, b]

Abstract: The synthesis and characterisation of the pro-ligand **LH4**, in which **L** is the *o*-phenylenebisamide-2-imidazole and its nickel(II) complexes are reported. The X-ray structures of the fully protonated [**NiLH2**] and deprotonated [**NiL**] complexes are presented. The effects of the deprotonation of the imidazole functions on the electronic structure of the complexes are analysed by ^{1}H NMR, UV/Vis and IR spectroscopy and cyclic voltammetry. Density functional theory (DFT) and time-dependent density functional theory (TDDFT) calculations support the analysis based on experimental data. The singly oxidised form of the deprotonated complex [**NiL**] was generated by preparative electrolysis and its electronic structure was investigated. Spectroelectrochemistry shows the appearance of intense transitions in the region $\lambda = 600$–900 nm with several isosbestic points. X-band EPR spectroscopy presents an isotropic signal at $g = 2.03$, whereas the Q-band EPR reveals a weak anisotropic signal characteristic of a metalloradical species. DFT and TDDFT data support the description of the species as a nickel(II)-radical form, with a major contribution of the spin density on the phenylene ring and the amidate functions with a negligible participation of the imidazolate groups. This finding is in sharp contrast with those obtained from the one-electron-oxidised form of nickel(II) complexes containing phenolate groups.[1–3]

Keywords: amides · density functional calculations · electrochemistry · imidazole · nickel · protonation

Introduction

The imidazole ring from the histidine amino acid residue is a common ligand found at the active sites of both metalloenzymes[4] and in metal free enzymes.[5] In metal-containing active sites, imidazole groups are commonly bound to the metal ions through the imino nitrogen atom. Their presence certainly regulates the redox potentials of the metal centre through the coordinating features of the imidazole ring. If imidazole groups are found in the region of the first coordination spheres, it is often postulated that they act in the regulation of substrate affinities. More subtly, Histidine 190, which is hydrogen-bound to a tyrosine Z residue at the heart of Photosystem II, is argued to play an essential role in the control of the redox properties of the tyrosine cofactor.[6,7] In the case of metal-free active sites such as fumarate reductase, histidine residues are thought to play roles, both as an anchoring site for the substrate and as a base for proton abstraction. The function of the imidazole ring of histidine differs in each situation. A recurrent question in natural systems concerns the protonic state of the metal bound histidyl imidazole ligands. It is assumed rightly that partial or complete deprotonation modulates the electronic and redox properties of the metal core, owing to the change in the ligand field strength. This issue is related to a more general concept in biology that there is no net charge accumulation at the active sites of metalloenzymes because the energetic penalty would be too high. The biological solution to this problem is to couple proton transfers with electron transfers.[8]

One facet of bioinorganic chemistry is to develop synthetic models so as to replicate the biological subtleties mentioned above. An elegant example by Valentine et al., reported that in a hexacoordinated iron(III)–porphyrin derivative, deprotonation of the axial imidazole ligands leads to a modification of the Fe^{III}/Fe^{II} couple redox potential by

---

[a] B. Lassalle-Kaiser, Dr. R. Guillot, J. Sainton, Dr. M.-F. Charlot,
Prof. A. Aukauloo
Institut de Chimie Moléculaire et des Matériaux d'Orsay
UMR-CNRS 8182, Université de Paris-Sud, F-91405 Orsay (France)
E-mail: mcharlot@icmmo.u-psud.fr
aukauloo@icmmo.u-psud.fr

[b] Prof. A. Aukauloo
Service de Bioénergétique, CEA Saclay
Bât. 532, 91191 Gif-sur- Yvette CEDEX (France)

Supporting information for this article is available on the WWW under http://www.chemeurj.org/ or from the author.

about 700 mV.[9] More recently, a reshuffling in electronic configuration of a high-spin iron(II)–porphyrin upon deprotonation of an axial imidazole ligand was reported.[10] These experimental facts clearly underlie the relationship between the nature of the imidazole ring and the electronic properties of metal porphyrinates. In the case of non-heme complexes, Williams and co-workers were the first to show a drastic drop in the redox potential of a non-porphyrinic iron complex upon deprotonation of four ligated imidazole moieties.[11] Analysis of the electrochemical data revealed a drop of around 300 mV shift per proton. However, attempts to elucidate the processes involved have been realised by using a coordinatively saturated iron complex to prevent any structural change in the coordination sphere of the metal ion. Indeed, one pitfall with synthetic imidazole ligands is that upon deprotonation the imidazolate group shifts from a monodentate mode to a bidentate bridging one.[12–14] For this reason, imidazole groups are incorporated in ligand scaffolds as their *N*-methyl derivative. Other derivatives, such as benzimidazole[15–17] or bisimidazoline[18] have also been used to tackle the same issue, that is to say the tuning of the redox properties coupled with remote proton abstraction.

In this paper we report on the synthesis of a novel ligand containing two amido and two imidazole groups. The nickel(II) complex has been prepared and both the neutral [**NiLH2**] and the dianionic [**NiL**] complexes have been characterised by X-ray diffraction techniques. The electrochemical behaviour is analysed as function of the protonic states of the imidazole rings and the monooxidised form of the deprotonated species has been characterised by spectroelectrochemistry as well as X and Q band EPR spectroscopy. As a rule of thumb, an approximate drop of 300 mV in the redox potential was observed per proton abstraction. We have used density functional theory (DFT) and time-dependent density functional theory (TDDFT) calculations to explain the electronic properties of both nickel(II) complexes and the singly oxidised form issued from [**NiL**].

Results

Synthesis of the ligand and nickel(II) complexes: Pro-ligand **LH4** and complexes [**NiLH2**] and [**NiL**] (see Scheme 1) were prepared as previously described.[19] The key molecule for the synthesis of **LH4** is the 2-imidazole acyl chloride. This molecule is obtained, according to a modified published procedure,[20] by reacting the hydrochloride salt of imidazole-2-carboxylic acid with oxalyl chloride in acetonitrile. Unidentified compounds were obtained if the non-protonated imidazole was used. The relatively stable imidazolium acyl chloride was isolated and then reacted with a stoichiometric amount of *o*-phenylenediamine in tetrahydrofuran (THF) in the presence of two equivalents of triethylamine (TEA) to give a beige solid with a yield of about 50%. Washing the solid with THF and water affords a pure compound. The ligand can be crystallised in a mixture of alkaline water and dimethylsulfoxide (DMSO). Insertion of the nickel(II) ion in the coordinating cavity was realised by reacting **LH4** with two (for [**NiLH2**]) or four (for [**NiL**]) equivalents of hydroxide salt in methanol (MeOH) and treating it with one equivalent of nickel(II) nitrate. The neutral complex [**NiLH2**] precipitated out of the reacting mixture and was isolated by filtration. Yellow crystals were obtained by air diffusion of water in a solution of [**NiLH2**] in DMSO. Complex [**NiL**] was prepared as the alkylammonium salt (NMe_4^+ or NBu_4^+). Thin orange needles were obtained by air diffusion of diethyl ether in a solution of [**NiL**]-$[NMe_4]_2$ in ethanol.

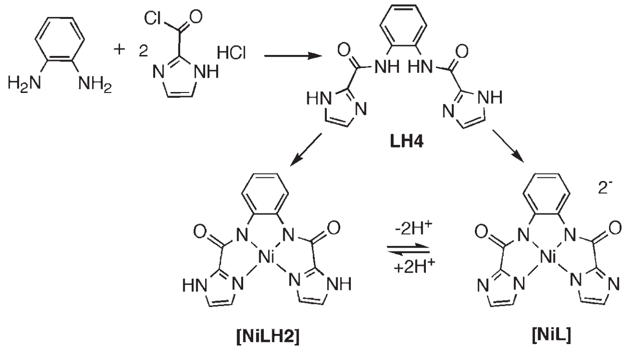

Scheme 1.

Spectroscopic characterisation:

^{1}H NMR spectroscopy: Changes in the charge density upon remote deprotonation of the imidazole groups were evidenced by proton NMR, as both complexes stay diamagnetic, even in coordinating solvents such as DMSO. As expected for the dianionic form [**NiL**], an upfield shift (around 1 ppm) of the imidazole protons was observed, reflecting an increase in the electron density on these groups. A more subtle effect towards higher field was seen for the protons in the *meta* positions to the amido groups. However, protons in the *ortho* positions of the amido group on the benzenic ring were not subjected to any change, this was attributed to the fact that these positions lie on the nodes of the frontier orbitals (see Table S1 in the Supporting Information).

UV/Vis spectroscopy: Spectral modifications of the electronic absorption spectra were also monitored upon deprotonation. The reversible changes were observed between $\lambda = 300$ and 450 nm. We will analyse these electronic transitions in the light of TDDFT calculations.

IR spectroscopy: Two main changes on the IR spectra were noticed upon deprotonation. The loss of the wide structured band in the region of $\tilde{\nu} = 3130–2430\ cm^{-1}$ from the neutral to the dianionic species indicates the loss of the hydrogen bonding in the solid state. More relevant to the inner coordination sphere is the noticeable shift ($\Delta\tilde{\nu} = 40\ cm^{-1}$) to higher frequencies of the C=O stretching modes in the case of the deprotonated complex. The reason for this is the enhancement of the charge transfer from the imidazolate and the deprotonated amido nitrogen atom into the NCO fragment.

X-ray structures: Crystals of sufficient quality were obtained for [**NiLH2**] and [**NiL**][NMe$_4$]$_2$·6H$_2$O and were characterised by X-ray diffraction techniques. The main structural changes within the coordination sphere of the nickel ion and the imidazole rings upon deprotonation are qualitatively displayed in Figure 1.

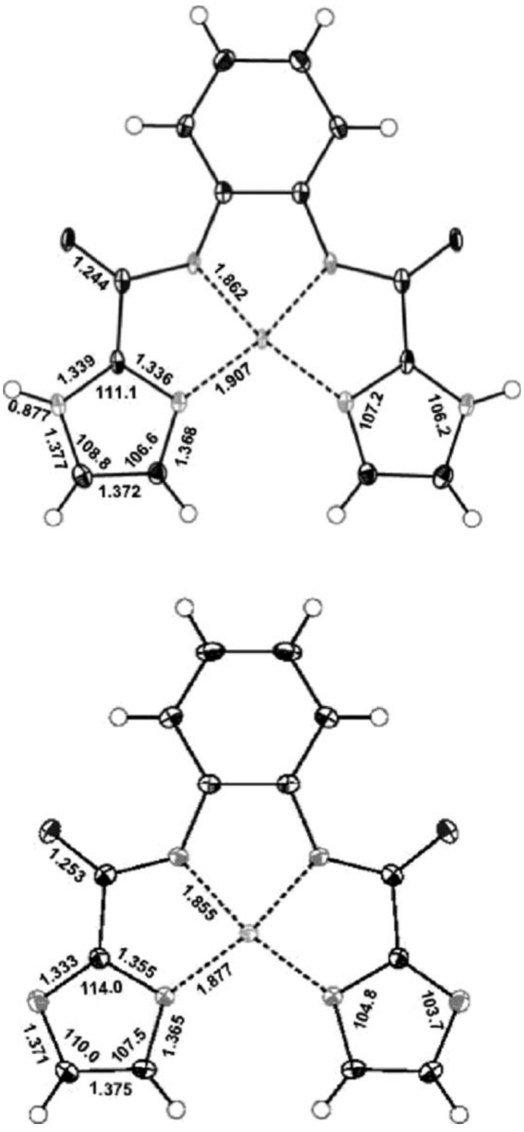

Figure 1. ORTEP diagram of [**NiLH2**] (top) and [**NiL**] (bottom) with selected bond length [Å] and angles [°]. Ellipsoid drawn at 50% probability.

As already observed, the changes in bond lengths and angles for the imidazole rings from [**NiLH2**] to [**NiL**] are attributed to the increase in bond delocalisation for the imidazolate ring. As expected, the stronger field strength of the imidazolate ring led to a contraction of the respective Ni−N bonds by about 0.03(0) Å. A shrinking of the Ni−N$_{amido}$ distances is also operating upon deprotonation of the imidazole, whereas an elongation of the C=O bonds is evidenced, concomitantly, as depicted in Figure 1. This metric data is in accord with the IR signatures and support the higher frequency shift of the C=O bond for the dianionic complex. The solid-state structure of [**NiLH2**] reveals the formation of an extended array of the constituting nickel monomer. In effect, the presence of the self-complementary functions, herein the NH group of the imidazole (proton donor) and the carbonyl amidate (proton acceptor) groups on the periphery of the nickel complex leads to a head-to-tail arrangement of contiguous monomers through a double hydrogen bond strap (see Figure 2).

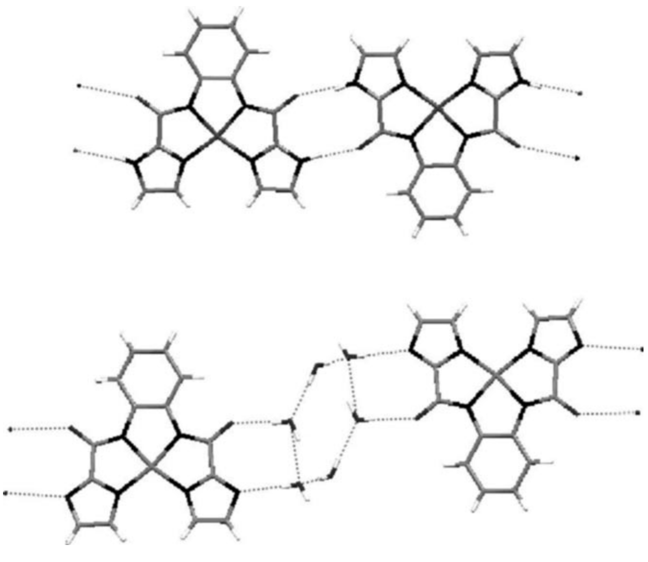

Figure 2. Hydrogen-bond network for [**NiLH2**] (top) and [**NiL**] (bottom).

The intermolecular hydrogen bond length (d[H···O] = 1.86(1) Å, d[N−H···O] = 2.72(9) Å) and the corresponding angle (θ[N−H···O] = 169°(7)) place these bonds into the class of moderate hydrogen bonds.[21]

A more intricate hydrogen-bonding network implicating water molecules of crystallisation is noted in the crystal structure of [**NiL**][NMe$_4$]$_2$·6H$_2$O (Figure 2). An extended water molecule array runs through the *ac* plane and connects the dianionic units among them. Along the *b* axis, three molecules of water link the nitrogen atom of the imidazolate group to the oxygen atom of the amide group of two consecutive molecules in a head-to-tail fashion. Notably, no intermolecular binding through the external nitrogen atom of the imidazolate is evidenced in the solid-state structure. This brings an additional proof that in this case deprotonation of the imidazole rings does not lead to the formation of extended or multinuclear discrete molecules.

Electrochemical behaviour: Cyclic voltammetry was carried out in DMSO for solubility reasons. Complex [**NiLH2**] shows a quasi-reversible reduction wave at $E=-1.85$ V vs saturated calomel electrode (SCE) ($\Delta E_p=60$ mV). On the anodic side of the CV two successive waves at $E_p=0.70$ and $E_p=0.87$ V vs SCE are detected. The first wave is irreversible in nature, whereas the second one is quasi-reversible ($\Delta E_p=120$ mV). Upon addition of two equivalents of potassium *tert*-butoxide (*t*BuOK) to the solution, a reversible wave is observed at $E=0.13$ V vs SCE ($\Delta E_p=70$ mV) (see Figure S1 in the Supporting Information). This wave falls in the same potential window as the $Ni^{III/II}$ couple for other tetraanionic ligands.[1,22–25] Therefore the difference of about 600 mV between the first anodic waves is consistent with the previously reported values for the deprotonation of a coordinated imidazole group[9,11] ($\approx$300 mV drop per proton). The corollary to this downshift of the first oxidation wave is the concomitant disappearance of the reduction wave observed at −1.88 V. Both of these changes observed for the electrochemical behaviour of the nickel(II) complex upon deprotonation demonstrate the higher field strength generated by the deprotonated imidazole groups.

One-electron-oxidised complex [NiL]ox: Attempts to oxidise and spectroscopically characterise the neutral complex were unfruitful in our hands. Bulk electrolysis was performed on a solution of the deprotonated complex in situ at 0.3 V vs SCE. The green solution formed is stable for hours under inert atmosphere, but decomposes more rapidly when exposed to air. The chemical reversibility of the oxidised species was confirmed by running a voltammogram after electrolysis (see Figure S2 in the Supporting Information) and by the presence of different isosbestic points when monitored by spectroelectrochemistry. The main spectral features of the one-electron-oxidised species are a broad band observed in the region $\lambda=600$–900 nm, as well as new electronic transitions in the near UV/Vis region. The origin of these bands will be discussed later through the use of TDDFT calculations.

The X-band EPR spectrum of the oxidised species was recorded at $T=80$ K and reveals an almost isotropic signal centred at around $g=2$ with a half width of about 100 G (see Figure 3). Addition of an exogenous coordinating ligand such as pyridine modifies the spectral pattern to an axial signal with *g*-values of 2.19 ($g_\perp$) and 2.02 ($g_\parallel$). The splitting of the $g_\parallel$ signal into 5 lines can be explained by examination of the superhyperfine coupling of the unpaired electron with two nitrogen atoms in the axial positions[26] (see Figure S3 in the Supporting Information). This observation indicates that the oxidised nickel complex can accommodate two axial ligands and that the unpaired electron in the case of the bis-adduct resides in a d_{z^2} type orbital. The anisotropy of the signal in absence of the axial binding ligands could only be resolved by running the Q-band EPR. A rhombic signal with $g_x=2.08$, $g_y=2.02$ and $g_z=2.00$ was detected ($g_{av}=2.033$). A mere comparison of these values with those of a genuine rhombic nickel(III) complex (for which the g values are observed mainly around 2.2[1,22,23,27,28]) clearly indicates that the generated **[NiL]ox** species is more of a metalloradical type species. As far as we are aware of, this is the first example of a nickel complex in a formal oxidation state greater than +II showing radical behaviour with imidazolate ligands in its coordination sphere. To gain insights into the proper electronic description of this novel family of complexes, we have performed DFT and TDDFT calculations. In the following section, we confront the computed data with the experimental ones.

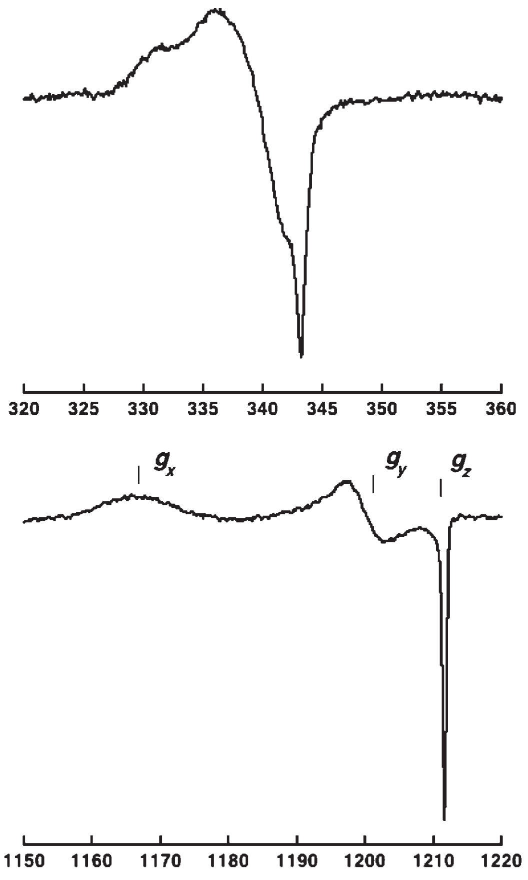

Figure 3. X- (top) and Q-band (bottom) EPR spectra recorded at 80 K of an electrochemically prepared solution of **[NiL]ox** in DMSO. Preparative electrolysis conditions : 2 mM in DMSO, TBAP 0.1 M, Glassy Carbon. X-band EPR recording conditions: 9.63 GHz microwave frequency, 0.03 mW microwave power, 0.25 mT modulation amplitude, 100 kHz modulation frequency. Q-band EPR recording conditions: 34 GHz microwave frequency, 2.3 mW microwave power, 0.5 mT modulation amplitude, 100 kHz modulation frequency.

Discussion

Complexes [NiLH2] and [NiL]

Optimised geometries: As a prerequiste to all DFT calculations using the B3LYP functional,[29] the optimised geometries of the isolated molecules were determined in C_2 point group with the choice of y as symmetry axis joining the Ni ion and the middle of the C−C bond between the ortho positions of the phenylene ring. The structures are almost planar (plane *xy*) and selected distances are reported in Table 1. As generally found, the bond distances calculated in vacuo are slightly larger than the experimental ones. The calculated Ni−N distances are shorter for the nitrogen of the *N*-amide (Ni−N_{am}) than toward the nitrogen of the imidazole (Ni−N_{im}) in agreement with the X-ray structures. The enhanced donating character of the deprotonated imidazole is observed experimentally, as the Ni−N_{im} bond is shorter in the deprotonated [**NiL**] complex than in [**NiLH2**]. Our computed data also accounts for the elongation of the C=O bond in [**NiL**] and, the higher frequency shift for these probes on the IR spectrum.

Table 1. Selected geometric parameters calculated in gas phase for [**NiLH2**], [**NiL**] and the oxidised complex [**NiL**]**ox**.

	[NiLH2]	[NiL]	[NiL]ox
distances [Å]			
Ni−N_{am}	1.882	1.882	1.863
Ni−N_{im}	1.933	1.909	1.881
C_{am}−O	1.264	1.269	1.253
C_{am}−C_{im}	1.482	1.484	1.463
angles [°]			
N_{am}−Ni−N'_{am}	84.5	85.2	84.6
N_{im}−Ni−N'_{im}	105.0	106.2	105.3

Energy levels and molecular orbitals: For the two complexes, the energy levels and molecular orbitals were calculated by DFT in a solvent medium modelled in the framework of a polarised dielectric-like continuum model (PCM).[30,31] As pointed out by the results, the presence of acetonitrile, a polar solvent with dielectric constant $\varepsilon = 36.64$, affects the total energy of the molecules. The deprotonated complex bearing a −2 total charge is much more stable than the neutral compound. In effect, the electrostatic polar solute–solvent contribution to the solvation energy is $-29\,\text{kcal}\,\text{mol}^{-1}$ for [**NiLH2**] and is as large as $-162\,\text{kcal}\,\text{mol}^{-1}$ for [**NiL**].

This calculation also affords the molecular orbitals that constitute the framework to the study of the excited states. Their energies and preponderant compositions are listed in Table S2 in the Supporting Information. The molecular orbital (MO) diagram for the ground state for both complexes (Figure 4) is typical of a low-spin square-planar Ni^{II} species with a ligand of large σ strength and d_{z^2} orbital encountered in the same energy range as the d_{xz} and the d_{yz} orbitals.

We notice that the two complexes are isoelectronic. Owing to its anionic nature, the orbitals of [**NiL**] are destabilised compared to those of [**NiLH2**]. However, their composition remains qualitatively similar. The *o*-phenylenebisamidate moiety possesses high-lying occupied π-orbitals, which can mix with the 3d orbitals of nickel. The highest of them (of *b* symmetry) constitutes the HOMO (MO 90) of both complexes with a small d_{yz} contribution. MO 89 is a d_{xz}-type orbital with the contribution of an *a* symmetry *o*-phenyleneamidate orbital; this mixing is strong in [**NiLH2**], in which the d_{xz} counterpart is encountered in MO 87, whereas the mixing is small in [**NiL**] in which MO 89 remains predominantly d_{xz}. In both complexes, MO 88 is a pure d_{z^2} orbital.

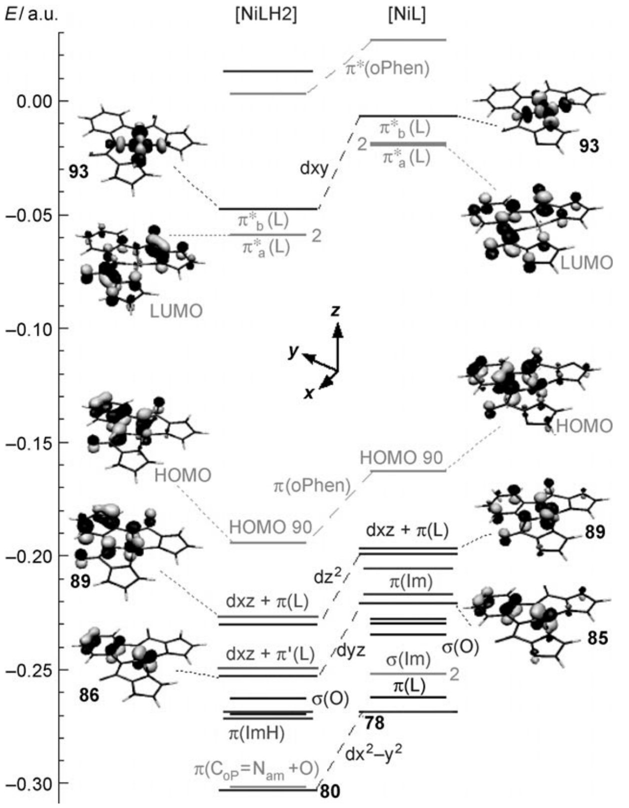

Figure 4. Energy level diagram (in atomic units: a.u.) of the MOs of [**NiLH2**] and [**NiL**] showing some typical obitals.

Our calculations demonstrate that the two complexes differ in the nature or ordering of the molecular orbitals lower in energy. The d_{yz}-type orbital of nickel, which mixes with a π-orbital on the phenylene cycle, occurs as MO 86 in [**NiLH2**] and MO 85 in [**NiL**], whereas the more stabilised in-plane $d_{x^2-y^2}$ orbital occurs as MO 80 and MO 78, respectively. The other orbitals have essentially ligand character. Among them we can distinguish delocalised orbitals, the combinations of the in-plane lone pairs on oxygen atoms and the combinations of π orbitals on the imidazole rings. The orbitals with contribution from the imidazolates are destabilised by about 1.6 eV compared to those of the protonated imidazoles as a consequence of the accumulation of electronic density in this region for [**NiL**]. Besides, two lone-pair orbitals of the imidazolate groups are encountered for [**NiL**] in this energy region.

Among the computed vacant orbitals, the two LUMOs π^*_a and π^*_b are delocalised ligand orbitals, with an important π-bonding character between the amide carbon and the carbon of the imidazole, whereas the vacant d_{xy} orbital of nickel (MO 93) lies above for both complexes. Notably, our theoretical data indicate a HOMO–LUMO energy gap smaller in [**NiLH2**] (3.68 eV) than in [**NiL**] (3.91 eV).

Electronic absorption spectra: The low-lying singlet excited states of the two complexes were studied in acetonitrile surrounding using PCM/TDDFT calculations, a method that describes these states in terms of monoexcitations from occupied to vacant MOs of the ground state. Selected transitions, excitation energy, wavelength, oscillator strength f and composition are reported in Tables S3 and S4 of the Supporting Information for [**NiLH2**] and [**NiL**], respectively. These data allow us to calculate the corresponding stick-spectra as shown in Figures 5 and 6 and to simulate the absorption spectra. Here a fwhm of 2000 cm^{-1} was used as spectral band-width. This value is smaller than the values observed in the experimental spectra. Nonetheless, it helps to visualise that in the two complexes several transitions of almost the same nature are sufficiently near in energy to give rise to a "band" with a definite label. Selected preponderant monoexcitations are also presented in Figure 5 and Figure 6 by using the isodensity plots of the involved MOs.

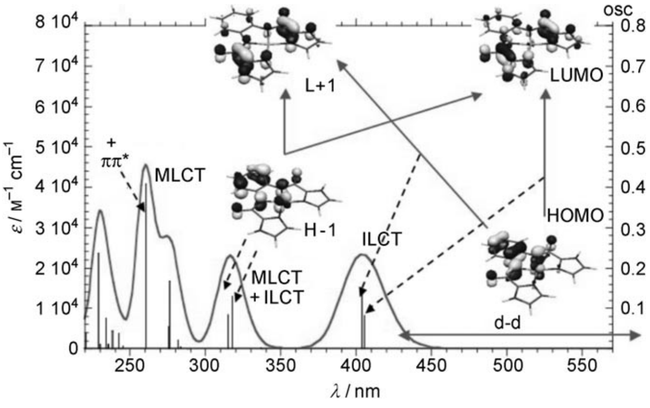

Figure 5. Calculated UV/Vis spectrum of [**NiLH2**]. Calculated stick-spectrum drawn according to TDDFT wavelengths and oscillator strengths and simulated spectrum obtained with a fwhm of 2000 cm^{-1}. Preponderant monoexcitations are presented using the isodensity plots of the involved MOs. Dominant character of the simulated bands is specified.

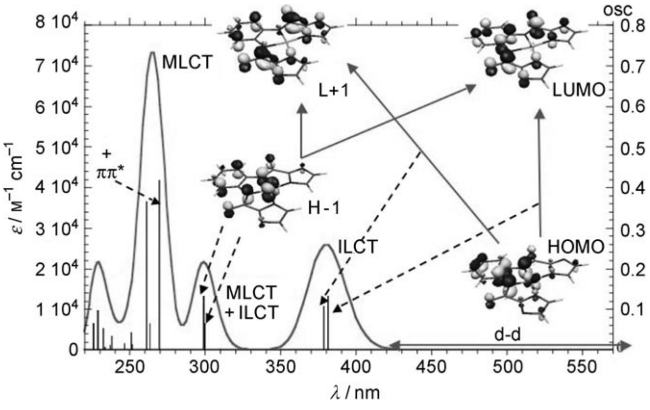

Figure 6. Calculated UV/Vis spectrum of [**NiL**]. Calculated stick-spectrum drawn according to TDDFT wavelengths and oscillator strengths and simulated spectrum obtained with a fwhm of 2000 cm^{-1}. Preponderant monoexcitations are presented using the isodensity plots of the involved MOs. Dominant character of the simulated bands is specified

The d–d transitions of vanishing intensity are computed between $\lambda = 428$ and 640 nm for [**NiLH2**] and between $\lambda = 412$ and 576 nm for [**NiL**]. Almost pure intraligand charge transfers (ILCT) from the *o*-phenylene part of the ligand to the ligand delocalised π^*_a and π^*_b orbitals with high electronic density in the $C_{im}-C_{am}=O$ region culminate around $\lambda = 405$ nm in [**NiLH2**] and 380 nm in [**NiL**], whereas the mixed-character ILCT+MLCT (metal-to-ligand charge transfer) absorptions are calculated around $\lambda = 315$ nm and 300 nm, respectively. Finally, transitions with an important metal-to-ligand character are encountered around $\lambda = 275$ nm for the complex with the neutral imidazole rings and $\lambda = 265$ nm for the complex with the deprotonated imidazoles. Intensity enhancement is observed in this region, owing to the presence of a π–π* excitation on the *o*-phenylene fragment. We notice that all these transitions have the same nature in both complexes and appear in the same wavelength order. However, all excitations are shifted to more energetic values for the dianionic complex, in connection with the increase of the HOMO–LUMO gap. In contrast ligand-to-metal charge transfers (LMCT) from the oxygen lone pairs are calculated at higher energy in the reverse order ie. at $\lambda = 242$ nm for [**NiLH2**] and at $\lambda = 251$ nm for [**NiL**]. The good agreement between the simulated and experimental spectra (see Figure S4 in the Supporting Information) already validates our theoretical methodology in the electronic description of the complexes.

Oxidised complex [NiL]ox: A more challenging task is the electronic description of the singly oxidised species [**NiL**]**ox**, as it is an open shell complex.

Nature of the oxidised state: UB3LYP geometry optimisations were performed in C_2 symmetry followed by integral-equation formalism version of the polarised-continuum model (IEF-PCM) calculations in acetonitrile at the resulting optimised geometry. A ^2B state is obtained and we have checked, by means of TDDFT, that it is actually the ground state of the singly oxidised form, that is, no negative excitation energy is calculated starting from this ^2B state. Its energy is calculated at 4.19 eV above the ground ^1A state of [**NiL**], each state being considered in its own geometry. An energy level diagram of the spin-orbitals of [**NiL**]**ox** in correlation to the MOs of [**NiL**] is reported in Figure S5 in the Supporting Information and some typical orbitals are shown.

The main information concerning the ^2B state are reflected on the spin density distribution map (Figure 7). By inspection of the electronic distribution of the α HOMO (Figure 7) and comparison to the HOMO of [**NiL**] in Figure 4, we can conclude that the oxidised ^2B state results from removal of one electron from the HOMO of the non oxidised complex, an orbital which was depicted as a π-orbital developed on the nitrogens of the *o*-phenylene and amido groups with only a small d_{yz} contribution. Upon analysis of the spin density distribution map, we infer that the ^2B state can be described as an organic radical with a small

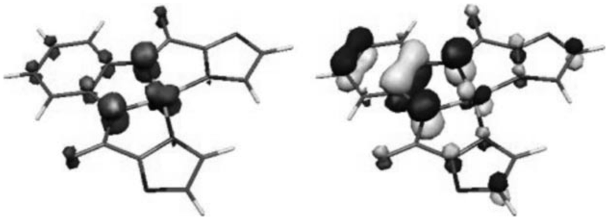

Figure 7. Ground ^{2}B state of the oxidised complex [**NiL**]**ox** calculated in acetonitrile. Spin density distribution (left, contour value 0.006 a.u.). Isodensity plot (right) of the αHOMO (contour value 0.05 a.u.).

metallic Ni^{III} character. Indeed, the Mulliken spin density on the nickel ion remains as small as 0.181 and amounts to 0.215 on each of NCO amidato fragment. A non-negligible contribution of 0.273 is also computed on the central *o*-phenylene cycle, whereas each imidazolate bears only 0.058 spin.

As we will define later, this description of the ^{2}B state has important spectroscopic consequences on the UV/Vis spectrum as well as on the EPR signature.

*Electronic absorption spectrum of [**NiL**]**ox***: Selected excited states for [**NiL**]**ox** are described in Table S5 of the Supporting Information and the simulated spectrum in the infra-red, visible and UV regions is reported in Figure 8.

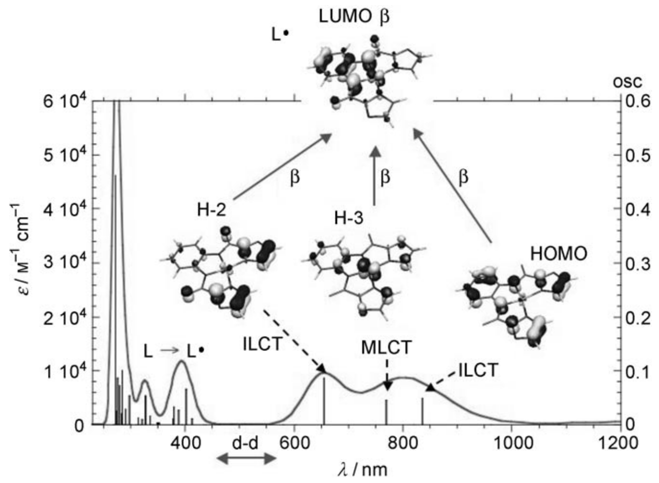

Figure 8. Calculated UV/Vis spectrum of [**NiL**]**ox**. Calculated stick-spectrum drawn according to TDDFT wavelengths and oscillator strengths and simulated spectrum obtained with a fwhm of 2000 cm^{-1}. Preponderant monoexcitations are presented using the isodensity plots of the involved spin-orbitals. Dominant character of the simulated bands is specified.

In the infra-red region, three transitions with non-zero intensity involve the population of the β LUMO. They are composed mainly of MLCT (state 7) or intraligand charge transfer (ILCT, states 5 and 8) transitions. By ILCT, we refer to the charge transfer from one localised fragment to another within the ligand skeleton, as shown in Figure 8. Using a fwhm of 2000 cm^{-1}, a resulting band ranging from $\lambda = 550$ to 1000 nm is simulated with two maxima around $\lambda =$ 650 and 800 nm. The d–d transitions with negligible intensity are calculated between $\lambda = 400$ and 510 cm^{-1} and transitions at higher energy present important mixing with π–π* character and involve either the whole ligand or only the central aromatic ring. These transitions are however not relevant in our study. A comparison of the experimental spectrum to the simulated one (using a more realistic fwhm of 3200 cm^{-1}) is presented in Figure 9. Surprisingly, an excellent agreement is reached, therefore bringing again extra support to the validation of our theoretical findings.

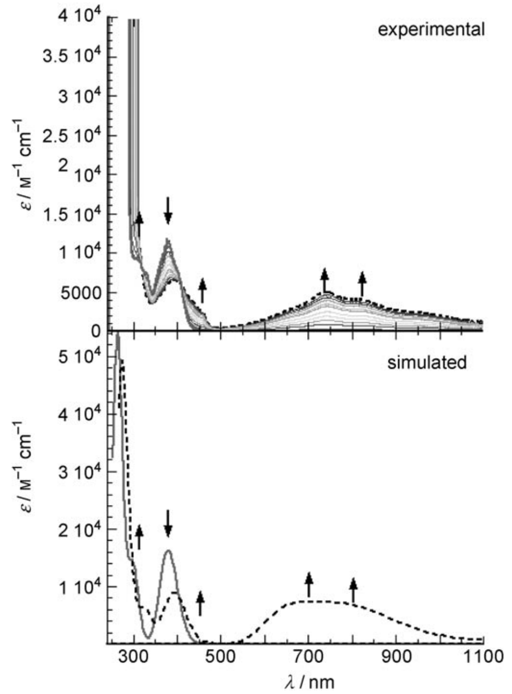

Figure 9. Comparison of simulated and experimental electronic spectra for [**NiL**] (full lines) and its [**NiL**]**ox** oxidised form (dashed lines). Experimental spectroelectrochemistry in DMSO by addition of 2 equiv of *t*BuOK. Simulated spectra with a fwhm of 3200 cm^{-1} which is a value in good agreement with the experimental one.

Now we will analyse the transitions calculated at lowest energy in the far infra-red region involving excitations to the vacant β LUMO (Table S5 in the Supporting Information). They have essentially MLCT character. The first one at $\lambda = 1262$ nm is described as the lifting of an electron from the d_{xz} orbital with ligand contribution and the second at $\lambda = 1205$ nm ($f \sim 0.$) is from the d_{z^2} orbital. These excitations are meaningful because the corresponding states, at 0.98 and 1.03 eV respectively in this geometry, are the lowest doublet states with metallic Ni^{III} character. We will focus our attention on them in the next section. The third transition in this region is a d–d transition involving both α and β excitations from d_{z^2} to d_{xy}. A large band ranging from $\lambda = 1050$ to 1600 nm of low intensity ($\varepsilon_{Max} = 450\,M^{-1}cm^{-1}$ for a fwhm of 2000 cm^{-1}) is also simulated (Figure S6 in the Supporting Information).

A comparative study: Interests in metalloradical complexes range from the bioinorganic field[32] to molecular material science.[33,34] In the bioinorganic field, these synthetic complexes are called to share the reactivity properties of a number of enzymes in which both the metal and the ligands at the active sites play a crucial role in the respective catalytic redox cycle. The participation of ligand in the redox chemistry of non-porphyrinic metal complexes has been tackled mainly with phenol containing ligands.[35–39] Although an increasing number of such complexes with different metal ions have been characterised, till now there has been no direct evidence of the participation of the redox active ligand in the reactivity pattern of these complexes. It is therefore necessary to have a profound knowledge of the electronic properties of these complexes in order to include such chemical information in the synthetic models of the so-called "radical enzymes".

Rotthaus et al. reported an analogue of the [**NiL**] complex with phenolate rings[1] instead of the imidazolate motifs described in our paper. It was shown that the oxidised form could be best described as a bound phenoxyl radical to a nickel(II) ion. The authors also reported the nature of the SOMO obtained from DFT calculations (in absence of solvent medium) as being mainly localised on the phenol rings with only a small contribution of the dπ orbitals of the metal centre. Interestingly, only a feeble contribution was observed on the amido groups.

This is a typical example to show the preponderant participation of the phenol rings in the description of an oxidised form of a nickel(II) complex. The same behaviour has been observed for the monooxidised form of nickel(II) salophen complexes ie. with two imino and two phenolate groups in the coordination sphere of the metal ion.[2,3,40] We observed, in contrast with the phenol containing ligands, a distinct difference in the spin density distribution map. As can be seen in Figure 7, the contribution of the imidazolate rings is very weak in the description of the SOMO (α HOMO). This is a main finding in this study. Indeed, it seems that an imidazolate ring is best described as an "innocent" organic partner in this family of ligands while taking into account the nature of the metal centre and the binding mode of the ligand. As we mentioned above phenol and imidazole rings are widely distributed at the active sites of enzymes. Based on our findings, we can postulate that imidazolate rings at the metal centre do not participate as the phenolate groups do, in the electronic description of the oxidised forms of metal complexes, but rather act as a redox potential tuner through the remote deprotonable aminic site.

Another unique electronic behaviour observed for the singly oxidised form of nickel(II) complexes with phenol-containing ligands, is the valence tautomeric phenomenon. This is nicely evidenced for the one-electron-oxidised form of salen type nickel(II) complexes through the EPR studies as a function of temperature.[40] Although a Ni^{III}–phenolate with a metal-centred state is evidenced at low temperature, increasing the temperature leads to a ligand-centred radical. An important piece of evidence for the proper description of the one-electron-oxidised form of Ni^{II}–bis(salicylidene)diamine derivatives was recently brought by the group of Stack.[3] Indeed, the X-ray crystallographic data are supportive of a nickel(II) ion bound to a phenoxyl radical. Furthermore, the authors argued that the observed valence tautomeric effect observed in this family of complexes is probably owed to an axial coordination on the metal centre at low temperature. DFT calculations also confirm a metal–phenoxyl radical form. An interesting electronic feature is the observation of intense low-energy band for the oxidised form. Time-dependent DFT (in presence of a solvent) show that these low-energy transitions involve delocalised π orbitals that are spread over the ligand skeleton and the metal in both fundamental and excited states.

A recent study of Rotthaus et al. also reports similar description of the ground state of the one-electron-oxidised form of a nickel(II)–*o*-hydroxybenzamidate complex, in which the imine groups were replaced by amidato functions. The electronic absorption data from DFT calculations (in absence of solvent) also reinforce the metal-radical description of the singly oxidised species and is quite similar to the oxidised form of the Ni^{II}–bis(salicylidene)diamine derivative.

An interesting result from our TDDFT data is the finding that the two first excited states have an important Ni^{III} character. After geometry optimisation of each state in the gas phase, we are able to define their nature looking at their spin density distribution calculated in CH_3CN (Figure 10). These two states possess effectively a strong Ni^{III} character. The first excited state is a ^{2}A state with the unpaired spin in d_{z^2} lying at 0.65 eV (when optimised in its own geometry), whereas a second one also of ^{2}A symmetry with the unpaired electron in the d_{xz} orbital and small delocalisation on the amidate fragments is found at 0.77 eV (when optimised in its own geometry). Their metallic character is confirmed by the high value of the Mulliken spin density on nickel: 0.805 for the first and 1.116 for the second. These transitions were not experimentally evidenced, in 1) because of the limit of the apparatus and 2) because of the low intensity of these bands in contrast to those observed for the phenolate-containing ligands. However, our computed results already tell us that in presence of an exogenous binding ligand, a probable reshuffling of these states will undergo, leading for instance to the stabilisation of the d_{z^2} orbital.

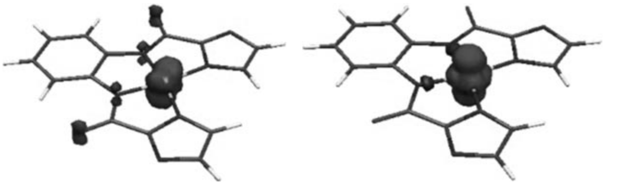

Figure 10. Spin density distribution for the excited states of [**NiL**]**ox** with Ni^{III} character: $^2A_{xz}$ (left) and $^2A_{z^2}$ (right).

Conclusion

In summary, we have shown how the remote deprotonation of imidazole fragments can alter the redox properties of a nickel(II) complex. The one-electron-oxidised form of the Ni–bis(amidateimidazolate) is best described as a ligand-radical complex. DFT analysis indicates that the imidazolate ligand contributes very little in the spin density distribution map, in sharp contrast with the phenolate-containing derivative.

Experimental Section

General procedures and methods: All reagents were obtained from commercial suppliers and used without purification unless specified. All NMR spectra were recorded by means of a Bruker DMX 400 MHz at room temperature. Solvents used are $CDCl_3$ ($\delta = 7.24$ ppm) or $[D_6]$DMSO ($\delta = 2.54$ ppm). ESI-MS spectra were recorded by means of a Finnigan MAT95S in a mixture of $CH_2Cl_2/MeOH/H_2O$ (1/1/1). IR spectra were recorded by means of a Fourier Transform Perkin–Elmer 883, using KBr solid solution (1% compound in mass). UV-Vis spectra were performed by means of a Varian CARY 50, in 1 mm optical way quartz cells. The EPR spectra were recorded on Bruker 200D (X band) and Bruker ELEXSYS 500 (Q band) spectrometers equipped with an Oxford Instrument continuous-flow liquid nitrogen cryostat and a temperature-control system. Cyclic voltammograms were recorded on a potentiostat-galvanostat 273 A EGG PAR, using a 3 mm^2 surface glassy carbon electrode. Bulk electrolysis were performed using a glassy carbon cylinder as working electrode. The electrolyte used is tetrabutylammonium perchlorate (TBAP) at a concentration of 0.1 M. Reference electrode is an Ag/$AgClO_4$ electrode (+ 0.53 V vs ENH, + 0.292 V vs ECS).

Imidazole-2-carboxylic acid hydrochloride salt: The commercially available imidazole-2-carboxylic acid (3 g, 26 mmol) was refluxed for half an hour in hydrochloric acid (35%, 10 mL). After cooling to room temperature, the solvents were evaporated. The white solid obtained was washed with acetone and filtered on a frit to again give a white solid (2 g, 8.6 mmol; yield = 65%). ^{1}H NMR ($[D_6]$DMSO, 250 MHz): $\delta = 7.68$ (s, 2H; C*H*), 13.10 (s, 1H; N*H*), 7.31 ppm (t, $J = 52$ Hz; 1H; NH^+); IR (KBr): $\tilde{\nu} = 579$, 615 (C–H), 1171 (C=O), 1637 (C=N), 3448 cm^{-1} (N–H, O–H).

Imidazole-2-acylchloride hydrochloride salt: Imidazole-2-carboxylic acid hydrochloride salt (345 mg, 2.33 mmol) was suspended in dry acetonitrile (5 mL). Oxalyl chloride (2.5 mL, 13 mmol; 6 equiv) was added under argon at 0 °C. While the suspension is heated to reflux for half an hour, a yellow solid was formed. After cooling to room temperature, of dry diethyl ether (20 mL) was added to the mixture, which was then filtered by a frit. The yellow solid obtained was washed with a minimum of cold acetonitrile and cold diethyl ether to afford the product (300 mg, 1.8 mmol; yield = 47%). ^{1}H NMR ($[D_6]$DMSO, 250 MHz): $\delta = 7.50$ (d, $J = 1.82$ Hz, 1H; C–*H*), 8.15 ppm (d, $J = 1.82$ Hz, 1H; C–*H*); IR (KBr): $\tilde{\nu} = 1278$ (C=O), 1741 (C=N), 3140 (N^+–H), 3458 cm^{-1} (N–H).

1,2-Bis(2-imidazolecarboxamido)benzene dihydrochloride (LH4·2HCl): Freshly distilled triethylamine (0.64 mL, 4.54 mmol) was added to a degassed solution of *o*-phenylenediamine (234 mg, 2.16 mmol) in distilled THF (10 mL), under argon. After 15 min stirring, the solution was transferred under argon into a flask containing imidazole-2-acyl chloride (715 mg, 4.28 mmol). The mixture was heated to reflux overnight under argon. The solvents were evaporated to dryness and the solid was quickly washed with water; a beige solid (400 mg, 1.0 mmol) was obtained (yield = 50%). ^{1}H NMR ($[D_6]$DMSO, 250 MHz): $\delta = 13.32$ (s, 4H; H–N_{imid}), 10.50 (s, 2H; H–N_{amid}), 7.70 (dd, $J_o = 6.00$ Hz, $J_m = 3.25$ Hz, 2H; H_o–Ph), 7.45 (s, 4H; *H*–Im), 7.32 ppm (dd, $J_o = 6.00$ Hz, $J_m = 3.25$ Hz, 2H; H_m–Ph); ^{13}C NMR ($[D_6]$DMSO, 250 MHz): $\delta = 153.6$ (2C, *C*=O), 138.7 (2C, C_{2Im}), 130.0 (2C, C_{1arom}), 126.8 (2C, C_{3arom}), 126.3 (2C, C_{2arom}) 122.7 ppm (4C, $C_{4,5Im}$); IR (KBr): $\tilde{\nu} = 3158$, 3127 (N_{imid}–H), 1686, 1647 ppm (C=O); ESI-MS: *m*/*z* (%) for [**LH4**Na]$^+$: 319 (100), 320 (17.7); elemental analysis calcd (%) for **LH4**·2HCl: C 45.54, H 3.82, N 22.76; found: C 43.76, H 3.81, N 21.90

Complex [NiLH2]: NaOH pellets (50 mg, 2 mmol) followed by $[Ni(NO_3)_2]\cdot 6H_2O$ (97 mg, 0.3 mmol) dissolved in a minimum of methanol (0.5 mL) were added to a suspension of **LH4**·2HCl (110 mg, 3×10^{-4} mol) in a minimum of methanol (3 mL). A deep yellow solid immediately precipitated, which was filtered by a frit and washed with methanol (yield = 90%; 95 mg, 0.27 mmol). ^{1}H NMR ($[D_6]$DMSO, 250 MHz): $\delta = 13.82$ (s, 2H; H–N_{imid}), 7.97 (dd, $J = 5.9$ Hz, $J' = 3.5$ Hz, 2H; *H*–Ph), 7.37 (s, 2H; *H*–Im), 7.25 (s, 2H; H–Im), 6.70 ppm (dd, $J = 5.9$ Hz, $J' = 3.5$ Hz, 2H; *H*–Ph); IR (KBr): $\tilde{\nu} = 3131$ (N_{imid}–H), 1614 cm^{-1} (C=O); elemental analysis calcd (%) for [**NiLH2**]$\cdot \frac{1}{2} H_2O$: C 46.45, H 3.06, N 23.22; found: C 46.41, H 2.66, N 23.47

Complex [NiL][NBu$_4$]$_2$: Bu_4NOH (40% in MeOH 1.62 mL, 2.27 mmol) followed by of $[Ni(NO_3)_2]\cdot 6H_2O$(106 mg, 0.36 mmol) were added to a suspension of **LH4**·2HCl (140 mg, 0.38 mmol) in a minimum of methanol (3 mL). A yellow suspension appeared after a few minutes stirring. The solvents were removed under vacuum and the resulting orange oil was stirred overnight in diethyl ether. The hygroscopic solid that formed was quickly filtered off, washed with diethyl ether and dried in a dessicator (yield = 83%; 250 mg, 3×10^{-4} mol); ^{1}H NMR ($[D_6]$DMSO, 250 MHz): $\delta = 8.01$ (dd, $J = 5.9$ Hz, $J' = 3.7$ Hz, 2H; *H*–Ph), 6.68 (s, 2H; *H*–Im), 6.58 (s, 2H; H–Im), 6.43 (dd, $J = 5.9$ Hz, $J' = 3.7$ Hz, 2H; *H*–Ph), 4.29 (t, $J = 7.9$ Hz, 16H; $N^+(CH_2$–Pr)), 4.09 (q, $J = 7.9$ Hz, 16H; N^+(Et–CH_2–Me)), 2.23 (q, $J = 6.7$ Hz, 16H; N^+(Me–CH_2–Et)), 1.8 ppm (t, $J = 6.7$ Hz, 24H; N^+(Pr–CH_3)); IR (KBr): $\tilde{\nu} = 1653$ (C=O); ESI-MS (negative): *m*/*z* (%): 350 (14.8), 351 (100), 352 (23.9), 353 (41.1), 354 cm^{-1} (9)

Crystallographic data collection and refinement of the structures of [NiLH2] and [NiL]: For [**NiLH2**], an orange crystal with approximate dimensions of 0.120 × 0.060 × 0.040 mm was selected. For [**NiL**], an orange crystal with approximate dimensions of 0.280 × 0.260 × 0.140 mm was selected. For the two compounds, diffraction collection was carried out on a kappa Bruker diffractometer equipped with an APEX II CCD detector. The lattice parameters were determined from 20 images recorded with 1° Φ scans and later refined on all data. The temperature of the crystal was maintained at the selected value (100 K) by means of a 700 series Cryostream cooling device to within an accuracy of ±1 K. Data were corrected for Lorentz polarisation. The structures were solved by direct methods by using SHELXS-97[41] and refined against F^2 by full-matrix least-squares techniques by using SHELXL-97[42] with anisotropic displacement parameters for all non-hydrogen atoms. Hydrogen atoms were located on a difference Fourier map and introduced into the calculations as a riding model with isotropic thermal parameters. Hydrogen of H_2O of [**NiL**] were refined. All calculations were performed by using the Crystal Structure crystallographic software package WINGX.[43]

Crystal [NiLH2]: formula = $C_{14}H_{10}N_6NiO_2$; $M_r = 352.97$, $T = 100(1)$ K, $\lambda = 0.71073$ Å; crystallographic system: orthorhombic; space group: *Pnna*; $a = 6.9007(7)$, $b = 9.3164(12)$, $c = 20.492(3)$ Å, $V = 1317.4(3)$ Å^3, $Z = 4$; $\rho = 1.780$ g cm^{-3}, $\mu = 1.494$ mm^{-1}, $\theta_{max} = 29.91°$; reflections measured: 5992; independent reflections: 1303; reflections observed with $I > 2\sigma(I)$: 1052 ($R_{int} = 0.0378$); parameters: 109; $R_1 = 0.0634$; $wR_2 = 0.0634$; $(\Delta/\sigma)_{max} = 0.002$, $\Delta\rho_{max} = 0.484$ e Å^{-3}, $\Delta\rho_{min} = -0.323$ e Å^{-3}.

Crystal [NiL]: formula = $C_{22}H_{44}N_8NiO_8$; $M_r = 607.34$, $T = 100(1)$ K, $\lambda = 0.71073$ Å; crystallographic system: orthorhombic; space group: *Pnma*; $a = 8.69660(10)$, $b = 30.1829(4)$, $c = 11.5575(2)$ Å, $V = 3033.71(7)$ Å^3, Z = 4; $\rho = 1.330$ g cm^{-3}, $\mu = 0.694$ mm^{-1}, $\theta_{max} = 41.87°$; reflections measured: 34036; independent reflections: 9135; reflections observed with $I > 2\sigma(I)$: 5978 ($R_{int} = 0.0391$); parameters: 202; $R_1 = 0.0439$; $wR_2 = 0.0955$; $(\Delta/\sigma)_{max} = 0.050$, $\Delta\rho_{max} = 0.658$ e Å^{-3}, $\Delta\rho_{min} = -0.672$ e Å^{-3}.

CCDC 663469 ([**NiLH2**]) and 663470 ([**NiL**]) contain the supplementary crystallographic data for this paper. These data can be obtained free of charge from The Cambridge Crystallographic Data Centre via www.ccdc.cam.ac.uk/data_request/cif.

Computation methods: Density functional theory calculations were carried out using Becke's three-parameter hybrid functional B3LYP[29] as implemented in the Gaussian 03 program package.[44] The valence triplezeta basis set including polarisation functions (TZVP) of Ahlrichs and coworkers[45,46] was used for the nickel ion and the double-zeta sets of the same authors were used for the other atoms. Spin-unrestricted UB3LYP calculations were performed for the doublet states of the oxidised complexes. For consistency reasons we did not use experimental structures but calculated geometries. Hence, in a first step, full geometry optimisations were carried out in vacuo for each complex. The C_2 symmetry constraints were fixed for [**NiLH2**] and [**NiL**] as well as for their oxidised forms. In a second step, solvation effects were then introduced in the framework of a self-consistent reaction field method. The medium was modelled in the integral equation formalism version of the polarised continuum model (IEF-PCM)[30,31] and acetonitrile was chosen as solvent as in the UV/Vis experiments. Parameters of the model—defining the shape of the solvent cavity and description of the solvent—were kept to their default value as implemented in the D.02 revision of Gaussian 03.[44] However, individual spheres were added on the imidazole hydrogen atoms (when present).

Time-dependent density functional calculations (TDDFT)[47] were performed to determine the energies and characters of the lowest vertical excitations retaining the spin multiplicity of the ground state. The UV/Vis spectra were next simulated by a sum of individual gaussian lineshapes with a value of $3200\,\mathrm{cm^{-1}}$ (≈ 0.40 eV) for the full-width at half-maximum (fwhm) and a band area proportional to the calculated oscillator strength. Such a value of the fwhm is used in similar simulations.[48,49]

Acknowledgement

This work was supported by the CNRS (ANR Blanc HYPHO) and the European Commission (NEST STREP SOLAR-H contract No. 516510).

[1] O. Rotthaus, O. Jarjayes, F. Thomas, C. Philouze, C. Perez Del Valle, E. Saint-Aman, J.-L. Pierre, *Chem. Eur. J.* **2006**, *12*, 2293–2302.

[2] L. Benisvy, R. Kannappan, Y.-F. Song, S. Milikisyants, M. Huber, I. Mutikainen, U. Turpeinen, P. Gamez, L. Bernasconi, E. J. Baerends, F. Hartl, J. Reedijk, *Eur. J. Inorg. Chem.* **2007**, 637–642.

[3] T. Storr, E. C. Wasinger, R. C. Pratt, T. D. P. Stack, *Angew. Chem.* **2007**, *119*, 5290–5293.

[4] A. Messerschmidt, R. Huber, T. Poulos, K. e. Wieghardt, *Handbook of Metalloproteins, Wiley-VCH* **2001**.

[5] M. K. Doherty, S. L. Pealing, C. S. Miles, R. Moysey, P. Taylor, M. D. Walkinshaw, G. A. Reid, S. K. Chapman, *Biochemistry* **2007**, *39*, 10695–10701.

[6] K. L. Westphal, C. Tommos, R. I. Cukier, G. T. Babcock, *Curr. Opin. Plant. Biol.* **2000**, *3*, 236–242.

[7] G. Renger, *Biochim. Biophys. Acta, Bioenerg.* **2004**, *1655*, 195–204.

[8] J. M. Mayer, I. J. Rhile, *Biochim. Biophys. Acta, Bioenerg.* **2004**, *1655*, 51–58.

[9] R. Quinn, C. E. Strouse, J. S. Valentine, *Inorg. Chem.* **1983**, *22*, 3934–3940.

[10] C. Hu, B. C. Noll, C. E. Schulz, W. R. Scheidt, *J. Am. Chem. Soc.* **2005**, *127*, 15018–15019.

[11] R. F. Carina, L. Verzegnassi, G. Bernardinelli, A. F. Williams, *Chem. Commun.* **1998**, 2681–2682.

[12] Y. Sunatsuki, Y. Motoda, N. Matsumoto, *Coord. Chem. Rev.* **2002**, *226*, 199–209.

[13] H. Ohtsu, Y. Shimazaki, A. Odani, O. Yamauchi, W. Mori, S. Itoh, S. Fukuzumi, *J. Am. Chem. Soc.* **2000**, *122*, 5733–5741.

[14] J. T. Landrum, D. Grimmett, K. J. Haller, W. R. Scheidt, C. A. Reed, *J. Am. Chem. Soc.* **1981**, *103*, 2640–2650.

[15] B. S. Hammes, M. T. Kieber-Emmons, R. Sommer, A. L. Rheingold, *Inorg. Chem.* **2002**, *41*, 1351–1353.

[16] M.-A. Haga, T.-A. Ano, K. Kano, S. Yamabe, *Inorg. Chem.* **1991**, *30*, 3843–3849.

[17] M.-A. Haga, *Compr. Coord. Chem. II* **2004**, *1*, 125–134.

[18] J. P. Roth, S. Lovell, J. M. Mayer, *J. Am. Chem. Soc.* **2000**, *122*, 5486–5498.

[19] B. Lassalle-Kaiser, R. Guillot, É. Anxolabéhère-Mallart, A. Aukauloo, *Tetrahedron Lett.* **2006**, *47*, 3379–3382.

[20] J. P. Collman, M. Bröring, L. Fu, M. Rapta, R. Schwenninger, *J. Org. Chem.* **1998**, *63*, 8084–8085.

[21] T. Steiner, *Angew. Chem.* **2002**, *114*, 50–80; *Angew. Chem. Int. Ed.* **2002**, *41*, 48–76.

[22] H.-J. Kruger, R. H. Holm, *Inorg. Chem.* **1987**, *26*, 3647–3649.

[23] T. J. Collins, T. R. Nichols, E. S. Uffelman, *J. Am. Chem. Soc.* **1991**, *113*, 4708–4709.

[24] X. Ottenwaelder, R. Ruiz-García, G. Blondin, R. Carasco, J. Cano, D. Lexa, Y. Journaux, A. Aukauloo, *Chem. Commun.* **2004**, 504–505.

[25] X. Ottenwaelder, A. Aukauloo, Y. Journaux, R. Carrasco, J. Cano, B. Cervera, I. Castro, S. Curreli, M. C. Munoz, A. L. Rosello, B. Soto, R. Ruiz-Garcia, *Dalton Trans.* **2005**, 2516–2526.

[26] F. V. Lovecchio, E. S. Gore, D. H. Busch, *J. Am. Chem. Soc.* **1973**, *95*, 3109–3118.

[27] C. Freire, B. de Castro, *J. Chem. Soc. Dalton Trans.* **1998**, 1491–1497.

[28] J. Hanss, H. Krüger, *Angew. Chem.* **1998**, *110*, 366–369; *Angew. Chem. Int. Ed.* **1998**, *37*, 360–363.

[29] A. D. Becke, *J. Chem. Phys.* **1993**, *98*, 5648.

[30] E. Cancès, B. Menucci, J. Tomasi, *J. Chem. Phys.* **1997**, *107*, 3032–3041.

[31] J. Tomasi, B. Mennucci, E. Cancès, *THEOCHEM* **1999**, *464*, 211–226.

[32] J. Stubbe, W. A. van der Donk, *Chem. Rev.* **1998**, *98*, 705–762.

[33] A. Caneschi, D. Gatteschi, R. Sessoli, P. Rey, *Acc. Chem. Res.* **1989**, *22*, 392–398.

[34] D. Luneau, P. Rey, *Coord. Chem. Rev.* **2005**, *249*, 2591–2611.

[35] A. Sokolowski, B. Adam, T. Weyhermüller, A. Kikuchi, K. Hildenbrand, R. Schnepf, P. Hildebrandt, E. Bill, K. Wieghardt, *Inorg. Chem.* **1997**, *36*, 3702–3710.

[36] A. Sokolowski, J. Müller, T. Weyhermüller, R. Schnepf, P. Hildebrandt, K. Hildenbrand, E. Bothe, K. Wieghardt, *J. Am. Chem. Soc.* **1997**, *119*, 8889–8900.

[37] B. Adam, E. Bill, E. Bothe, B. Goerdt, G. Haselhorst, K. Hildenbrand, A. Sokolowski, S. Steenken, T. Weyhermüller, K. Wieghardt, *Chem. Eur. J.* **1997**, *3*, 308–319.

[38] J. Müller, A. Kikuchi, E. Bill, T. Weyhermüller, P. Hildebrandt, L. Ould-Moussa, K. Wieghardt, *Inorg. chim. acta* **2000**, *297*, 265–277.

[39] L. Benisvy, E. Bill, A. J. Blake, D. Collison, E. S. Davies, C. D. Garner, G. McArdle, E. J. L. McInnes, J. McMaster, S. H. K. Rossa, C. Wilsona, *Dalton Trans.* **2006**, 258–267.

[40] Y. Shimazaki, F. Tani, K. Fukui, Y. Naruta, O. Yamauchi, *J. Am. Chem. Soc.* **2003**, *125*, 10512–10513.

[41] G. M. Sheldrick, SHELXS-97, Program for Crystal Structure Solution, University of Göttingen, Göttingen, Germany **1997**.

[42] G. M. Sheldrick, SHELXL-97, Program for the refinement of crystal structures from diffraction data, University of Göttingen, Göttingen, Germany **1997**.

[43] L. J. Farrugia, *J. Appl. Crystallogr.* **1999**, *32*, 837–838.

[44] M. J. Frisch, G. W. Trucks, H. B. Schlegel, G. E. Scuseria, M. A. Robb, J. R. Cheeseman, J. A. Montgomery, Jr., T. Vreven, K. N. Kudin, J. C. Burant, J. M. Millam, S. S. Iyengar, J. Tomasi, V. Barone, B. Mennucci, M. Cossi, G. Scalmani, N. Rega, G. A. Petersson, H. Nakatsuji, M. Hada, M. Ehara, K. Toyota, R. Fukuda, J. Hasegawa, M. Ishida, T. Nakajima, Y. Honda, O. Kitao, H. Nakai, M. Klene, X. Li, J. E. Knox, H. P. Hratchian, J. B. Cross, V. Bakken, C. Adamo, J. Jaramillo, R. Gomperts, R. E. Stratmann, O. Yazyev, A. J. Austin, R. Cammi, C. Pomelli, J. W. Ochterski, P. Y. Ayala, K. Morokuma, G. A. Voth, P. Salvador, J. J. Dannenberg, V. G. Zakrzewski, S. Dapprich, A. D. Daniels, M. C. Strain, O. Farkas, D. K. Malick, A. D. Rabuck, K. Raghavachari, J. B. Foresman, J. V. Ortiz, Q. Cui, A. G. Baboul, S. Clifford, J. Cioslowski, B. B. Stefanov, G. Liu, A. Liashenko, P. Piskorz, I. Komaromi, R. L. Martin, D. J. Fox, T. Keith, M. A. Al-Laham, C. Y. Peng, A. Nanayakkara, M. Challacombe, P. M. W. Gill, B. Johnson, W. Chen, M. W. Wong, C. Gonza-

lez, J. A. Pople in *Gaussian 03*, *Revision D.02*, *Vol.* Gaussian, Wallingford CT, **2004**.

[45] A. Schaefer, H. Horn, R. Ahlrichs, *J. Chem. Phys.* **1992**, *97*, 2571.

[46] A. Schaefer, C. Huber, R. Ahlrichs, *J. Chem. Phys.* **1994**, *100*, 5829.

[47] M. E. Casida, C. Jamorski, K. C. Casida, D. R. Salahub, *J. Chem. Phys.* **1998**, *108*, 4439–4449.

[48] A. Gabrielsson, P. Matousek, M. Towrie, F. Hartl, S. Zalis, A. Vlcek, Jr, *J. Phys. Chem. A* **2005**, *109*, 6147–6153.

[49] S. R. Stoyanov, J. M. Villegas, D. P. Rillema, *Inorg. Chem. Commun.* **2004**, *7*, 838–841.

Received: October 22, 2007